Chinese Journal of Natural Medicines

Kaurepenoid A, a 2–*nor*–*ent*–kaurane diterpenoid with P–glycoprotein–mediated reversal of multidrug resistance activity from the fungus *Bipolaris* sp.

Yong Shen, Nanjin Ding, Meijia Zheng, Tianyuan Guo, Xiaoxia Gu, Yu Liang, Chunmei Chen, Qin Li, Yonghui Zhang, Hucheng Zhu

Citation: Yong Shen, Nanjin Ding, Meijia Zheng, Tianyuan Guo, Xiaoxia Gu, Yu Liang, Chunmei Chen, Qin Li, Yonghui Zhang, Hucheng Zhu, Kaurepenoid A, a 2–*nor*–*ent*–kaurane diterpenoid with P–glycoprotein–mediated reversal of multidrug resistance activity from the fungus *Bipolaris* sp., Chinese Journal of Natural Medicines, 2026, 24(10), 1251–1261. doi: 10.1016/S1875–5364(26)61218–6.

View online: https://doi.org/10.1016/S1875–5364(26)61218–6

Related articles that may interest you

Antimalarial and neuroprotective *ent*–abietane diterpenoids from the aerial parts of *Phlogacanthus curviflorus*

Chinese Journal of Natural Medicines. 2023, 21(8), 619–630 https://doi.org/10.1016/S1875–5364(23)60464–9

New pimarane diterpenoids with antibacterial activity from fungus *Arthrinium* sp. ZS03

Chinese Journal of Natural Medicines. 2024, 22(4), 356–364 https://doi.org/10.1016/S1875–5364(24)60629–1

New *nor*–*ent*–halimane and *nor*–clerodane diterpenes from *Callicarpa integerrima* with anti–MRSA activity

Chinese Journal of Natural Medicines. 2024, 22(11), 1003–1010 https://doi.org/10.1016/S1875–5364(24)60575–3

2,3–*Seco* and 3–*nor* guaianolides from *Achillea alpina* with antidiabetic activity

Chinese Journal of Natural Medicines. 2023, 21(8), 610–618 https://doi.org/10.1016/S1875–5364(23)60411–X

A 75 kDa glycoprotein isolated from *Cudrania tricuspidata* Bureau induces colonic epithelial proliferation and ameliorates mouse colitis induced by dextran sulfate sodium

Chinese Journal of Natural Medicines. 2021, 19(1), 46–55 https://doi.org/10.1016/S1875–5364(21)60005–5

New antibacterial depsidones from an ant–derived fungus *Spiromastix* sp. MY–1

Chinese Journal of Natural Medicines. 2022, 20(8), 627–632 https://doi.org/10.1016/S1875–5364(22)60170–5

Wechat

Chinese Journal of Natural Medicines 24 (2026) 1251-1261

Contents lists available at ScienceDirect

Chinese Journal of Natural Medicines

journal homepage: www.cjnmcpu.com/

Original article

Kaurepenoid A, a 2-*nor*-*ent*-kaurane diterpenoid with P-glycoprotein-mediated reversal of multidrug resistance activity from the fungus *Bipolaris* sp.

Yong Shen[a,Δ], Nanjin Ding[a,Δ], Meijia Zheng[a,b,Δ], Tianyuan Guo[a], Xiaoxia Gu[a], Yu Liang[a,c], Chunmei Chen[a], Qin Li[a,*], Yonghui Zhang[a,*], Hucheng Zhu[a,*]

[a] *Hubei Key Laboratory of Natural Medicinal Chemistry and Resource Evaluation, School of Pharmacy, Tongji Medical College, Huazhong University of Science and Technology, Wuhan 430030, China*

[b] *Department of Pharmacy, Union Hospital, Tongji Medical College, Huazhong University of Science and Technology, Wuhan 430022, China*

[c] *Department of Pharmacy, The Central Hospital of Wuhan, Tongji Medical College, Huazhong University of Science and Technology, Wuhan 430014, China*

ARTICLE INFO

Article history:
Received 11 April 2026
Revised 19 June 2026
Accepted 21 June 2026
Available online 20 October 2026

Keywords:
Bipolaris sp.
Ent-kaurane
Derivatization
Multidrug resistance
P-glycoprotein

ABSTRACT

Chemical research on the fungus *Bipolaris* sp. led to the identification of seven *ent*-kaurane diterpenoids, kaurepenoids A–G (**1**–**7**), marking the first isolation of such diterpenoids from this genus. Kaurepenoids A–F (**1**–**6**) represent the first 2-*nor*-*ent*-kaurane diterpenoids with a fused 5/6/6/5 tetracyclic ring system. Kaurepenoid G (**7**) bears a rare 2,3-epoxy-*ent*-kaurane skeleton. Their structures and absolute configurations were elucidated by NMR, ECD calculations, and single-crystal X-ray diffraction analyses. Putative biosynthetic pathways for kaurepenoids A–F were proposed. Furthermore, the derivatization of both kaurepenoids B and C as starting materials afforded five derivatives (**8**–**12**). Among these compounds, kaurepenoid A could increase the efficacy of anticancer drug paclitaxel (PTX) by 204-fold at 20 μmol·L^{-1}. Mechanistic investigation demonstrated that kaurepenoid A could inhibit the transport function of P-glycoprotein (P-gp) rather than affecting its expression, and the possible recognition mechanism was predicted by molecular docking.

1. Introduction

Ent-kauranoids are a class of typical tetracyclic diterpenoids, formed by a perhydrophenanthrene subunit and a cyclopentane [1]. To date, the number of *ent*-kauranoids from natural resources has exceeded 1000 members, mainly separated from the higher plants of the genus *Isodon* [2-8]. The oxidation, C–C bond cleavage, degradation, and rearrangement within the tetracyclic backbone of *ent*-kaurane increased their great potential in possessing fascinating skeletons, such as phyllastachysin M [9], maoecrystal V [10], and crokonoid A [11]. Additionally, bioactive diversity of *ent*-kauranoids, including cytotoxic [12-14], antibacterial [15], antiviral [13], antithrombotic [16], and anti-inflammatory [17-22], has also been revealed by previous research. The unusual structure, coupled with the significant pharmacology of *ent*-kauranoids renders them attractive synthetic targets [23-32].

Tumor multidrug resistance (MDR) is one of the leading causes of clinical chemotherapy failure, and the overexpression of P-gp is a central mechanism leading to the emergence and progression of MDR [33]. Among diverse *ent*-kauranoids, oridonin has been verified to possess tumor MDR reversal activity *via* corresponding regulatory effects [34]. For example, in human cisplatin-resistant SGC7901 cells, treatment with 10 μmol·L^{-1} oridonin alone effectively downregulates the expression levels of P-gp, MRP1, and cyclin D1; furthermore, the combination of oridonin with cisplatin synergistically reduces the IC_{50} of cisplatin [35].

The fungal genus *Bipolaris* is widespread in nature and has been proven to be a prolific producer of structurally diverse secondary metabolites, including sesquiterpenoids [36-38], diterpenoids [39], sesterterpenoids [40-42], meroterpenoids [43-45], and polyketides [46, 47], many of which exhibit significant biological activities such as immunosuppressive [48-50], anti-inflammatory [51], antimicrobial [44], phytotoxic [52], and MDR reversal activities [42]. In our ongoing investigation into the secondary metabolites of *Bipolaris* sp., seven previously undescribed *ent*-kauranoids were isolated and identified (Fig. 1). Among them, kaurepenoids A–F were presumed to form through 2,3-cleavage, C-2 degradation, and subsequent 1,3-cyclization on the basic *ent*-kauranoid skeleton, resulting in an unprecedented 2,3-*seco*-2-*nor*-1,3-cyclo-*ent*-kaurane scaffold. The ability of these compounds to reverse MDR to PTX in SW620/AD300 cell lines was also evaluated. Moreover, a set of derivatives was synthesized to elucidate the structure-activity relationship (SAR) of these compounds. Herein, the detailed structure elucidation, plausible biosynthetic pathway, derivative synthesis, and bioactivity evaluation of these isolates are presented.

2. Results and discussion

Kaurepenoid A (**1**) was obtained as colorless blocks. It had a molecular formula of $C_{24}H_{32}O_6$, requiring nine degrees of unsaturation, as deduced by the HR-ESI-MS data (*m/z* 439.2088 [M +

* Corresponding author.
E-mail addresses: liqin2023@hust.edu.cn (Q. Li); zhangyh@mails.tjmu.edu.cn (Y. Zhang); zhuhucheng@hust.edu.cn (H. Zhu)
Δ These authors contributed equally to this work.

https://doi.org/10.1016/S1875-5364(26)61218-6
Copyright © 2026, China Pharmaceutical University. Published by Elsevier B.V. All rights are reserved.

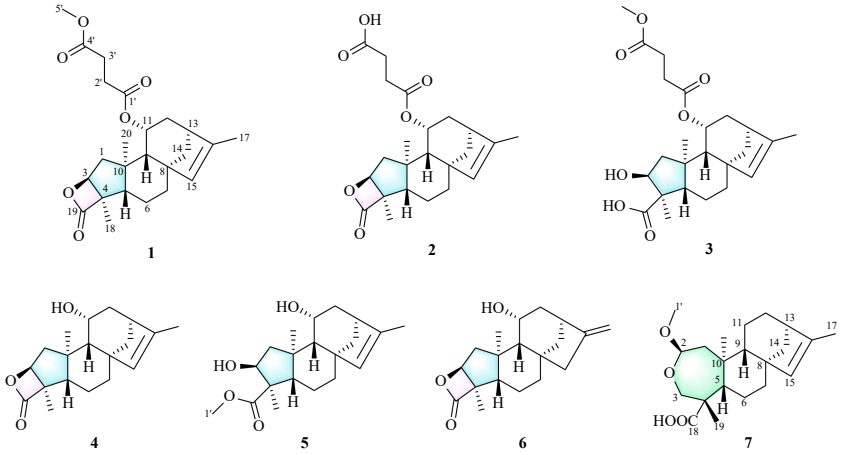


Fig. 1 Chemical structures of **1**–**7**.

Na]$^+$, Calcd. for $C_{24}H_{32}O_6Na$, 439.2097). In the ^1H NMR spectrum, typical resonances for three methyls (δ_H 1.10, s; 1.36, s; and 1.73, br s), one methoxyl (δ_H 3.69, s), and three downfield signals (δ_H 4.79, dd, J = 6.8, 3.5 Hz; 5.11, br s; and 5.22, dt, J = 11.2, 7.7 Hz) were revealed. The ^{13}C NMR data (Table 1) and DEPT spectra of **1** showed 24 carbon signals, ascribed for three methyls (δ_C 13.3, 15.6, and 20.4), one methoxyl (δ_C 52.1), seven methylenes (δ_C 19.5, 29.0, 29.9, 30.2, 38.0, 44.4, and 48.1), five methines including two oxygenated (δ_C 72.8 and 85.1), three nonprotonated carbons (δ_C 50.3, 53.6, and 63.0), two olefinic carbons (δ_C 133.8 and 143.8), and three ester-carbonyls (δ_C 171.8, 172.8, and 175.1). The aforementioned data suggested that compound **1** was a *nor*-

Table 1 ^1H and ^{13}C NMR data for compounds **1**–**3** in $CDCl_3$ (δ in ppm, J in Hz).

No.	**1**[b]		**2**[c]		**3**[c]	
	δ_H	δ_C	δ_H	δ_C	δ_H	δ_C
1	a 2.47 dd (13.6, 6.8) b 1.49[a]	48.1	a 2.46 dd (13.6, 6.8) b 1.47 m	48.0	a 2.51 dd (12.1, 6.6) b 1.18 m	52.4
3	4.79 dd (6.8, 3.5)	85.1	4.77 dd (6.8, 3.5)	85.1	4.22 t (7.8)	82.3
4		63.0		62.9		53.2
5	1.94 m	52.9	1.93 m	52.9	2.20 m	56.3
6	a 1.67[a] b 1.45 m	19.5	a 1.65 m b 1.45 m	19.4	a 1.42 m b 1.37 m	19.8
7	1.67[a]	38.0	1.66[a]	38.0	a 1.72 m b 1.59 m	38.7
8		50.3		50.3		50.4
9	1.93 m	50.0	1.92 m	50.0	1.83 d (8.3)	51.6
10		53.6		53.5		43.6
11	5.22 dt (11.2, 7.7)	72.8	5.21 dt (11.2, 7.6)	72.9	5.23 dt (11.1, 7.7)	72.9
12	a 1.98 m b 1.49[a]	30.2	a 1.96 m b 1.49 m	30.1	a 1.96 m b 1.54 m	30.4
13	2.44 q (3.8)	43.8	2.43 m	43.8	2.42 q (3.5)	44.0
14	a 2.09 d (10.6) b 1.37 m	44.4	a 2.08 d (10.6) b 1.35 m	44.4	a 2.16 d (11.0) b 1.32 m	44.4
15	5.11 br s	133.8	5.10 br s	133.7	5.10 br s	134.4
16		143.8		143.7		143.4
17	1.73 br s	15.6	1.72 br s	15.5	1.72 br s	15.5
18	1.36 s	13.3	1.34 s	13.2	1.26 s	19.6
19		175.1		175.2		181.3
20	1.10 s	20.4	1.09 br s	20.3	1.19 s	20.5
1′		171.8		171.6		172.0
2′	2.63[a]	29.0	2.65[a]	29.0	2.62[a]	29.1
3′	2.63[a]	29.9	2.64[a]	29.6	2.64[a]	29.9
4′		172.8		177.8		173.0
5′	3.69 s	52.1			3.69 s	52.0

[a]Overlapped; [b]Recorded at 600 (^1H NMR) and 150 (^{13}C NMR) MHz; [c]Recorded at 400 (^1H NMR) and 100 (^{13}C NMR) MHz.

diterpenoid [9, 53]. More detailed structural information was obtained by 2D NMR spectral analyses.

^{1}H–^{1}H COSY correlations (Fig. 2) of H-5/H_2-6/H_2-7 and H-9/H-11/H_2-12/H-13/H_2-14, and HMBC correlations (Fig. 2) from H_3-17 to C-13, C-15, and C-16, from H_2-14 to C-8 and C-15, from H_3-20 to C-5, C-9, and C-10, and from H-9 to C-7, C-8, and C-14, established rings C, D, and E. ^{1}H–^{1}H COSY correlations of H_2-1/H-3 and HMBC correlations from H_3-20 to C-1, C-5, and C-10, and from H_3-18 to C-3, C-4, and C-5, suggested that a five-membered ring B was fused with ring C *via* C-5 and C-10. The above identified functional groups and ring systems suggested that compound **1** possesses an extra ring. Furthermore, based on HMBC correlations from H_3-18 to C-3, C-4, and C-19, together with the chemical shifts observed for deshielded C-3 (δc 85.1) and shielded C-19 (δc 175.1) [54], a unique β-lactone ring was established and assigned as ring A, which is fused to ring B *via* the C-3 and C-4 positions. Moreover, the distinct downfield shift of C-11 (δ_C 72.8), combined with the HMBC correlations from H_3-5′ to C-4′, from H_2-2′ to C-4′, from H_2-3′ to C-1′, and from H-11 to C-1′ (δ_C 171.8), indicated that a monomethyl succinate group was attached to C-11 *via* an ester group. Thus, the planar structure of **1** was assigned as a 2-*nor*-*ent*-kaurane diterpenoid with a rare 5/6/6/5 tetracyclic carbon skeleton, bearing an additional β-lactone moiety.

The relative configuration of **1** was determined by analyzing its NOESY spectrum. Initially, the correlations (Fig. 3) of H_3-20/H-3/H_3-18 assigned the α-configurations of H-3, CH_3-18, and CH_3-20. Furthermore, the cross peaks of H_3-20/H-14a/H-12b, H-9/H-11, and H-11/H_3-17 disclosed that H-9 and H-11 were β-oriented, while both C-8 and C-13 were established as *S** configurations. Finally, single crystals suitable for X-ray crystallographic analysis were obtained (Fig. 4), which not only validated the planar structure of **1** but also determined its absolute configuration as 3*S*,4*R*,5*S*,8*S*,9*S*,10*R*,11*R*,13*S*.

Kaurepenoid B (**2**) was purified as colorless blocks with a molecular formula of $C_{23}H_{30}O_6$, as determined by the HR-ESI-MS data (*m/z* 425.1939 $[M + Na]^+$, Calcd. for $C_{23}H_{30}O_6Na$, 425.1940). The ^{1}H and ^{13}C NMR data (Table 1) of **2** closely resembled those of **1**, with the primary difference being the absence of a methoxy signal at C-4′ in the succinyl moiety, as corroborated by the deshielded chemical shift at C-4′ (δ_C 177.8). The NOESY spectrum of **2** revealed that compounds **2** and **1** possessed the same relative configuration. Finally, the absolute configuration of **2** was established as 3*S*,4*R*,5*S*,8*S*,9*S*,10*R*,11*R*,13*S* by single-crystal X-ray diffraction (Fig. 4).

Kaurepenoid C (**3**), obtained as colorless blocks, was assigned a molecular formula of $C_{24}H_{34}O_7$ based on the HR-ESI-MS data (*m/z* 457.2201 $[M + Na]^+$, Calcd. for $C_{24}H_{34}O_7Na$, 457.2202). The NMR data (Table 1) indicated that compound **3** was structurally similar to **1**. However, in comparison to **1**, the ^{13}C NMR spectrum of **3** showed an upfield shift for C-3 (δ_C 82.3) and a downfield shift for C-19 (δ_C 181.3). These observations suggested that the β-lactone ring in **1** underwent ring-opening, thereby giving rise to **3**. The relative configuration of **3** was determined by

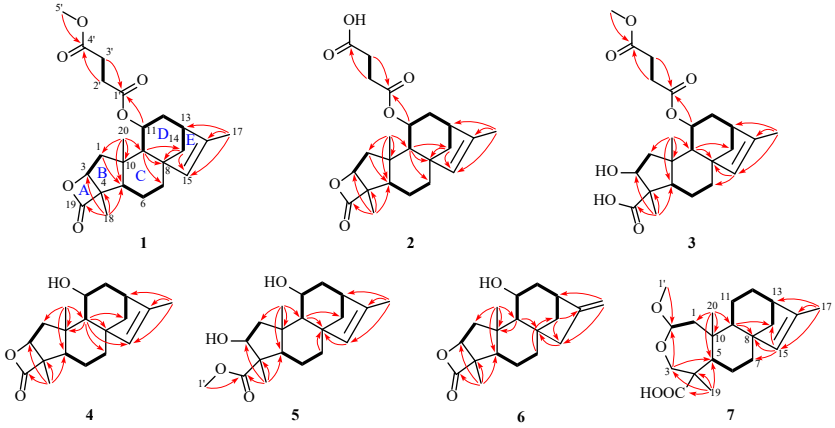


Fig. 2 The ^{1}H–^{1}H COSY (bold) and key HMBC (arrow) correlations of **1**–**7**.

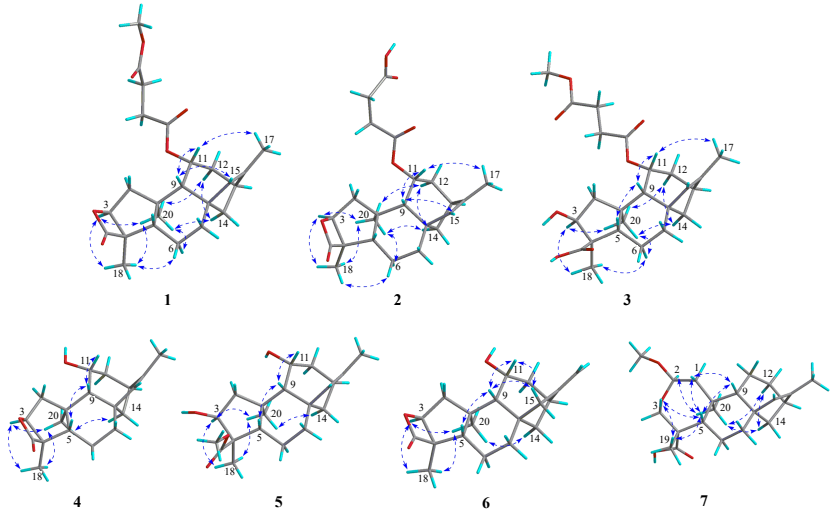


Fig. 3 The key NOESY correlations of **1**–**7**.

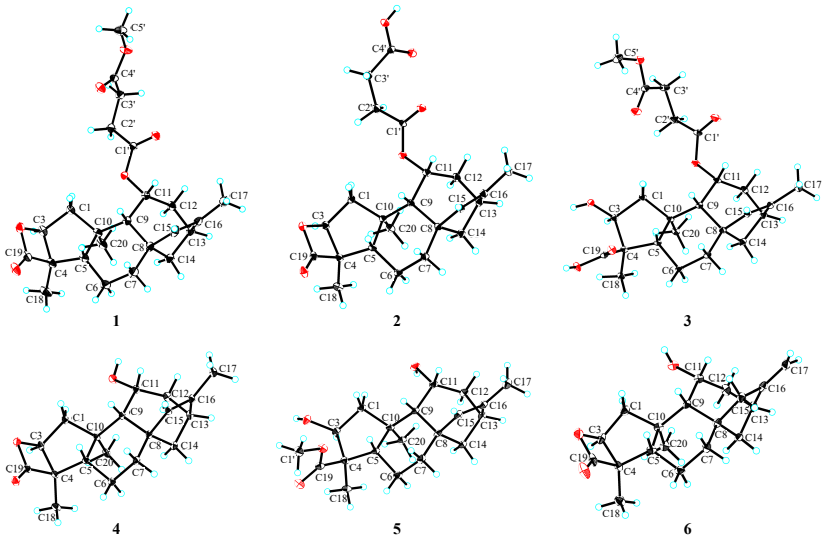


Fig. 4 X-ray crystallographic structures of **1**–**6**.

NOESY correlations (Fig. 3). The correlations of H_3-20/H-3, H-3/H_3-18, H_3-18/H-6a, and H-6a/H_3-20 indicated that these protons were cofacial and assigned an *α*-orientation. Meanwhile, correlations of H-5/H-9, H-9/H-11, and H-11/H_3-17 suggested that H-5, H-9, and H-11 were *β*-oriented, and cross peaks of H_3-20/H-14a/H-12a further determined the *S** configurations of C-8 and C-13. Finally, the absolute configuration of **3** was assigned as 3*S*,4*R*,5*S*,8*S*,9*S*,10*R*,11*R*,13*S* by X-ray crystallographic data (Fig. 4).

Kaurepenoid D (**4**) was gained as colorless blocks. Its molecular formula was determined to be $C_{19}H_{26}O_3$ based on the HR-ESI-MS data (*m/z* 325.1778 [M + Na]$^+$, Calcd. for $C_{19}H_{26}O_3Na$, 325.1780). The ^{1}H and ^{13}C NMR data (Table 2) of **4** were notably simpler compared to those of **2**, lacking the signals attributed to the succinyl moiety. The planar structure of **4** was further confirmed by ^{1}H–^{1}H COSY and HMBC correlations (Fig. 2). Finally, single-crystal X-ray diffraction analysis using Cu K*α* radiation es-

Table 2 ^{1}H and ^{13}C NMR data for compounds **4**–**7** in $CDCl_3$ (*δ* in ppm, *J* in Hz).

No.	**4**[b]		**5**[b]		**6**[b]		**7**[c]	
	δ_H	δ_C	δ_H	δ_C	δ_H	δ_C	δ_H	δ_C
1	a 2.76 dd (13.7, 6.8) b 1.57 m	49.1	a 2.77 dd (12.0, 6.7) b 1.26 m	53.8	a 2.72 m b 1.60 m	49.1	a 2.17 dd (15.6, 4.9) b 1.39 m	45.1
2							4.66 dd (9.8, 4.9)	101.1
3	4.80 dd (6.8, 3.6)	85.6	4.19 dd (8.8, 6.7)	82.6	4.81 dd (6.7, 3.6)	85.8	3.78[a]	66.8
4		62.9		53.5		62.6		49.6
5	1.95 dd (12.6, 2.7)	53.2	2.20 m	56.9	1.98 dd (12.5, 2.4)	53.5	1.06 dd (11.8, 3.1)	61.9
6	a 1.65[a] b 1.44 m	19.6	1.39[a]	20.0	a 1.67 m b 1.51 m	20.4	a 1.83 m b 1.74 dq (14.4, 3.1)	22.5
7	1.65[a]	38.2	a 1.71 m b 1.59 m	38.9	1.62[a]	40.2	a 1.55[a] b 1.44 m	39.6
8		50.2		50.3		45.3		49.6
9	1.80 dd (8.0, 1.2)	52.3	1.69[a]	54.2	1.86 d (7.1)	58.4	0.94 d (8.5)	45.6
10		53.8		43.5		53.8		42.8
11	4.10 dt (11.0, 7.6)	70.2	4.11 m	70.4	4.25 dt (12.1, 7.1)	68.9	a 1.64 m b 1.55[a]	20.8
12	a 1.94 m b 1.47 m	33.9	a 1.97 m b 1.51 ddd (13.2, 11.1, 2.5)	33.7	a 1.86 m b 1.74 dd (12.1, 2.4)	41.7	a 1.52 m b 1.46 m	25.3
13	2.43 d (6.0)	44.1	2.42 m	44.2	2.71 m	42.8	2.34 dt (5.5, 2.9)	44.5
14	a 2.07 d (10.5) b 1.33 m	44.7	a 2.13 d (10.5) b 1.30 m	44.6	a 2.01 d (11.8) b 1.12 ddt (11.8, 5.0, 1.6)	40.1	a 2.00 d (10.2) b 1.37 m	44.1
15	5.05 br s	133.9	5.04 br s	134.4	2.11[a]	48.0	5.06 br s	134.7
16		143.5		143.3		154.0		143.2
17	1.71 br s	15.5	1.70 br s	15.5	a 4.86 br s b 4.75 br s	104.3	1.69 br s	15.6
18	1.36 s	13.4	1.25 s	19.6	1.37 s	13.5		179.1
19		175.6		177.3		175.5	1.19 s	24.5
20	1.08 br s	20.3	1.17 s	20.7	1.07 br s	20.1	1.17 s	15.7
1′			3.72 s	52.2			3.35 s	55.1

[a]Overlapped; [b]Recorded at 400 (^{1}H NMR) and 100 (^{13}C NMR) MHz; [c]Recorded at 600 (^{1}H NMR) and 150 (^{13}C NMR) MHz.

tablished the absolute configuration of **4**.

Kaurepenoid E (**5**) was purified as colorless blocks, and its molecular formula was determined to be $C_{20}H_{30}O_4$ based on the HR-ESI-MS data (*m/z* 357.2053 [M + Na]$^+$, Calcd. for $C_{20}H_{30}O_4Na$, 357.2042). The ^1H and ^{13}C NMR data (Table 2) of **5** were similar to those of **4**, with the key difference arising from the ring opening of *β*-lactone and subsequent methyl esterification. The shielded effect at C-3 (δ_C 82.6) and the deshielded effect at C-19 (δ_C 177.3), together with the HMBC correlation (Fig. 2) from H_3-1′ (δ_H 3.72) to C-19, confirmed the above structural assignment. Furthermore, the relative configuration of **5** was assigned by NOESY correlations (Fig. 3). Eventually, the X-ray diffraction analysis of **5** established its absolute configuration.

Kaurepenoid F (**6**) was isolated as colorless needles with the same molecular formula as that of **4**. The ^1H and ^{13}C NMR data (Table 2) of **6** closely resembled those of **4**, with the primary distinction being the migration of the double bond from Δ^{15} in **4** to $\Delta^{16,17}$ in **6**, as evidenced by the HMBC correlations (Fig. 2) from H_2-17 to C-13 and C-15. Furthermore, NOESY correlations (Fig. 3) of H-15/H-11/H-9, H-9/H-5, H-3/H_3-20/H_3-18, and H_3-20/H-14a established the relative configuration of **6** as 3*S**,4*R**,5*S**,8*S**,9*R**,10*R**,11*R**,13*S**. Finally, the absolute configuration of **6** was determined by X-ray diffraction analysis.

Kaurepenoid G (**7**) was obtained as white powder with a molecular formula of $C_{21}H_{32}O_4$, as suggested by the HR-ESI-MS data (*m/z* 371.2202 [M + Na]$^+$, Calcd. for $C_{21}H_{32}O_4Na$, 371.2198). The ^1H NMR data (Table 2) of **7** displayed three methyl groups (δ_H 1.17, s; 1.19, s; and 1.69, br s), one methoxy group (δ_H 3.35, s), and four deshielded proton signals (δ_H 3.78, overlapped for two protons; 4.66, dd, *J* = 9.8, 4.9 Hz; and 5.06, br s). Its ^{13}C NMR data (Table 2) and DEPT spectra suggested the presence of three methyls (δ_C 15.6, 15.7, and 24.5), one methoxyl (δ_C 55.1), seven methylenes including one oxygenated (δ_C 66.8), four methines including one oxygenated (δ_C 101.1), and three nonprotonated carbons (δ_C 42.8, 49.6, and 49.6), two olefinic carbons (δ_C 134.7 and 143.2), and one carbonyl (δ_C 179.1). The spectral data of **7** closely matched those of previously isolated compounds, differing primarily in the structure of ring B. Rings C–E, with double bond $\Delta^{15,16}$, were established by the ^1H–^1H COSY and HMBC correlations (Fig. 2). Furthermore, a seven-membered oxygen ring B was established by the HMBC correlations from H_3-19 to C-3, C-4, C-5, and C-18, from H_2-3 to C-2 and C-5, from H_3-20 to C-1, C-5, and C-10, and from H_3-1′ to C-2, along with ^1H–^1H COSY correlations of H_2-1/H-2. Therefore, the planar structure of **7**, a 2,3-epoxy-*ent*-kauranoid, was assigned.

The relative configuration of **7** was deduced from the NOESY spectrum. The cross-peaks (Fig. 3) of H-1b/H-5/H-9, H_3-19/H-5/H-3, and H-2/H_3-20 indicated that H-5, H-9, and CH_3-19 were *β*-oriented, while H-2 and CH_3-20 were *α*-oriented. Furthermore, the cross-peaks of H_3-20/H-14a/H-12b suggested that C-8 and C-13 were *S** and *R** configurations, respectively. Eventually, the absolute configuration of **7** was determined as 2*R*,4*S*,5*S*,8*S*,9*S*,10*S*,13*R* by ECD calculation (Fig. 5).

Compounds **1**–**6** represented a novel class of 2-*nor*-*ent*-kauranoids, which were biosynthetically derived from *ent*-kaurane [55], as shown in Scheme 1. The proposed pathway started with the oxidation at C2/C3 positions of *ent*-kaurane, affording intermediate **i**. Subsequent C2–C3 bond cleavage converted **i** into intermediate **ii**, which then underwent aldol condensation to give intermediate **iii**. The oxidation and decarboxylation of **iii** afforded intermediate **v**, which was subsequently oxidized to yield intermediate **vii**. Intermediate **vii** could be transformed through two pathways: one underwent intramolecular esterification to yield compound **6**, and the other proceeded *via* double-bond isomerization to give intermediate **viii**. Intermediate **viii** had multiple subsequent reaction routes: firstly, intermediate **viii** was esterified with succinic acid to generate intermediate **ix**, which was further esterified to obtain compound **3**; secondly, intermediate

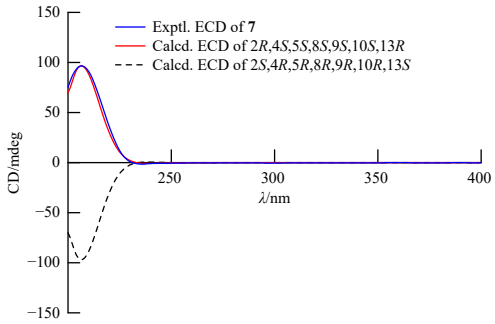
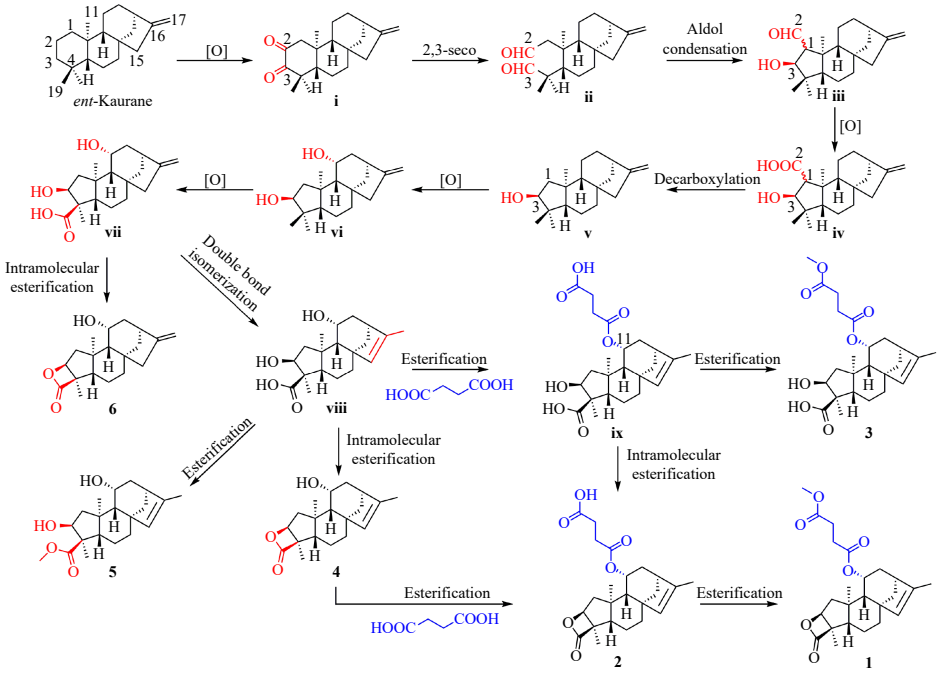


Fig. 5 Experimental and calculated ECD spectra of **7**.



Scheme 1 Plausible biosynthetic pathways of **1**–**6**.

viii was directly converted into compound **4** *via* intramolecular esterification, compound **4** was then esterified with succinic acid to yield compound **2**, and compound **2** was subsequently esterified to form compound **1**; additionally, intermediate **viii** could also be directly converted into compound **5** through esterification.

In bioassay, the MDR cell line SW620/AD300 was used to evaluate the efficacy of these isolated compounds against MDR *in vitro*. Firstly, the cytotoxic effects of compounds **1**–**7**, in combination with PTX on SW620/AD300 cells were tested by Cell counting kit-8 assay [42]. As shown in Table S1, after 72 h of treatment with PTX (1 μmol·L^{-1}) plus compound **1** (20 μmol·L^{-1}), SW620/AD300 cells showed a low viability, which revealed that compound **1** had the potential in reversing MDR. Most importantly, the reversal effect of compound **1** was remarkably superior to that of the positive control verapamil (VPM). The above results demonstrated that the concurrent existence of the *β*-lactone ring and the succinic acid moiety is essential for conferring activity. However, the structural comparison between compounds **1** and **2** reveals that esterification of the carboxyl group at C-4′ can significantly enhance the activity of compounds. Therefore, we first synthesized four different esterification products using compound **2** as a precursor (Fig. 6). However, none of these analogs (**8**–**11**) showed a significant improvement in MDR activity compared to **1** (Table S1). These findings indicate that increasing the size and hydrophobicity of the ester group at C-4′ is not beneficial. Simultaneously, to further confirm the effect of *β*-lactone ring, compound **12** was synthesized from compound **3**, yet this modification did not yield improved activity. Therefore, compound **1** was ultimately selected as an effective lead candidate for reversing tumor MDR.

Firstly, the colony formation assay suggested that compound **1** combined with PTX significantly inhibited the proliferation of SW620/AD300 cells, even PTX at the concentration of 0.25 μmol·L^{-1} (Figs. 7A and 7B). Furthermore, the impact of compound **1** on the cell cycle progression of SW620/AD300 cells was assessed by flow cytometry. The result showed that the combination treatment of compound **1** (20 μmol·L^{-1}) and PTX caused a decrease in G_1 phase (from 35% to 20%) and S phase (from 45% to 27%), and an increase in G_2/M phase (from 15% to 47%) in SW620/AD300 cells (Figs. 7C and 7D).

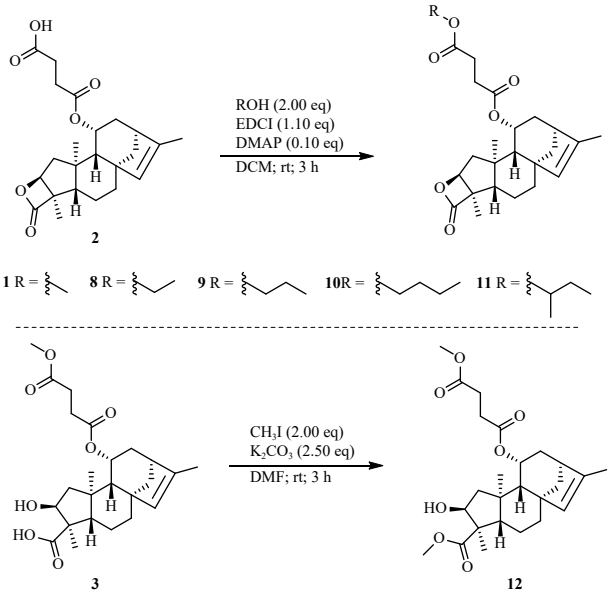


Fig. 6 The synthesis of **1** and **8**–**12**.

Moreover, to confirm the MDR reversal ability of compound **1** was related to P-gp modulation mechanism, the effect of compound **1** on the expression of P-gp in SW620/AD300 cells was explored. The result indicated that compound **1** at 20 μmol·L^{-1} did not affect the P-gp expression (Fig. 7G). Then Rhodamine123 (Rho123) accumulation assay was conducted to detect the efflux function of P-gp under the effect of compound **1**. The results showed that compound **1** dose-dependently increased the intracellular accumulation of Rho123, a substrate of the P-gp efflux

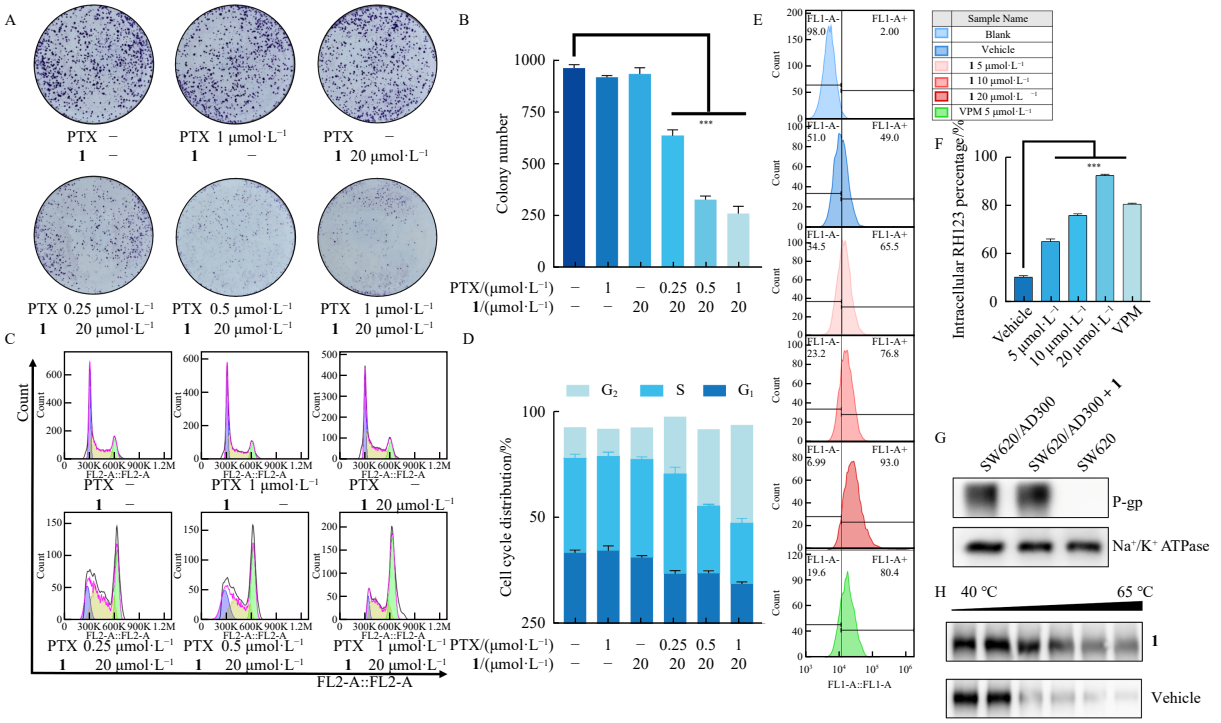


Fig. 7 Effects of **1** on the cell proliferative, cell cycle, and Rho123 accumulation of SW620/AD300 cells, and the thermal stability of P-gp. (A and B) Images and quantitative analysis of SW620/AD300 cells colony after treatment with PTX, **1**, or combination. (C and D) Flow cytometry analysis of the cell cycle in SW620/AD300 cells after treatment with PTX, **1**, or combination. (E and F) Analysis of Rho123 accumulation of **1** in SW620/AD300 cells by flow cytometry. (G) Expression levels of P-gp in SW620/AD300, SW620/AD300 (treated with **1**), and SW620. Na^+/K^+ ATPase was used as the loading control. (H) Melting graph of P-gp in CETSA treated with **1**. Data are presented as the mean ± SD, $n = 3$. $^{***}P < 0.001$ *vs* NC.

pump (Figs. 7E and 7F). These findings suggested that compound **1** could enhance the sensitivity of SW620/AD300 cells to PTX *via* the inhibition of P-gp. To determine whether compound **1** could directly bind to P-gp at the molecular level, the cellular thermal shift assay (CETSA) was conducted to explore the target engagement of compound **1** to P-gp in SW620/AD300 cells. As shown in Fig. 7H, compound **1** could significantly enhance the thermal stability of P-gp, even at a high temperature (65 °C), while P-gp in the vehicle group was largely degraded at this temperature. These results indicated that **1** could be a potential P-gp inhibitor.

Meanwhile, molecular docking was performed between P-gp (PDB model 7A6E) and compound **1**. Using the complex structure of P-gp with the inhibitor tariquidar as a reference, one molecule of **1** was docked into the vestibule between the binding pocket and the access tunnel of P-gp, which suggested that compound **1** formed a stable complex with P-gp with a binding affinity of –6.799 kcal·mol^{-1} (Fig. 8). Additionally, the docking results indicated that compound **1** formed three hydrogen bonds (H-bonds) with Trp232 (TM4), Gln347 (TM6), and Gln990 (TM12), and an aromatic H-bond with Trp232 (Fig. 8).

Based on the above research, we established a xenograft model bearing P-gp-overexpressing SW620/AD300 cells in nude mice to detect the reversal activity of compound **1** *in vivo*. The mice were treated with Vehicle, PTX, PTX plus VPM, and PTX plus compound **1**, respectively. The results showed that the combination of compound **1** and PTX could significantly reduce the tumor weight and volume of nude mice compared to PTX alone or vehicle control, even better than VPM (Figs. 9A–9C). Additionally, no significant body weight loss was observed at the tested dose, indicating that compound **1** was well tolerated in mice (Fig. 9D). Meanwhile, the HE and TUNEL analysis of tumor tissues (Figs. 9E and 9F) showed that the co-administration of compound **1** and PTX not only enhanced the death (nuclear pyknosis, vacuoles in HE staining) and apoptosis (bright green in TUNEL staining) of tumor cells, but also showed no increase in hepatotoxicity and nephrotoxicity. These results suggested that compound **1** could effectively reverse drug resistance *in vivo* and *in vitro*, making it a highly promising and safe candidate for combination therapy with PTX.

3. Conclusion

In conclusion, seven previously undescribed *ent*-kaurane diterpenoids were isolated and identified from the fungus *Bipolaris* sp. Among them, kaurepenoids A–F (**1**–**6**) were the first reported 2,3-*seco*-2-*nor*-1,3-cyclo-*ent*-kauranoids, with several (compounds **1**, **2**, **4**, and **6**) featuring a distinctive *β*-lactone ring. Kaurepenoid G (**7**) had a rare 2,3-epoxy-*ent*-kaurane skeleton. In bioassay, kaurepenoid A reversed the resistance of SW620/AD300 cells to PTX with a reversal fold of 204. Further SAR studies revealed that the *β*-lactone ring and the monomethyl succinate group are key pharmacophores. The presence of both is indispensable for the compounds to exhibit potent reversal of PTX resistance in MDR cells, while the absence of either one leads to a significant reduction or complete loss of activity. Thus, our research not only expand the diversity of *ent*-kauranoids, but also provide a significant target in the search for novel lead compounds to overcome PTX resistance.

4. Experimental

4.1. General experimental procedures

Optical rotations were measured on a Rudolph Autopol IV

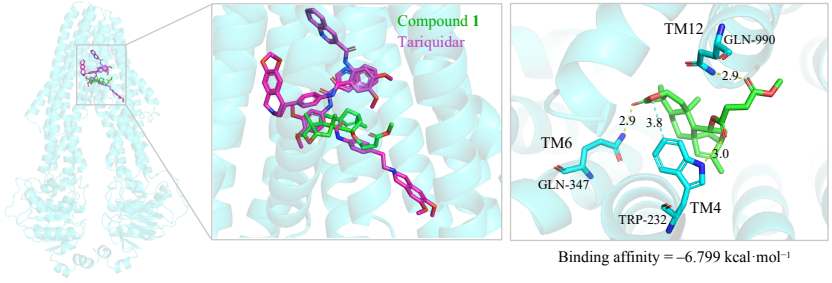


Fig. 8 Molecular docking result of **1** with P-gp.

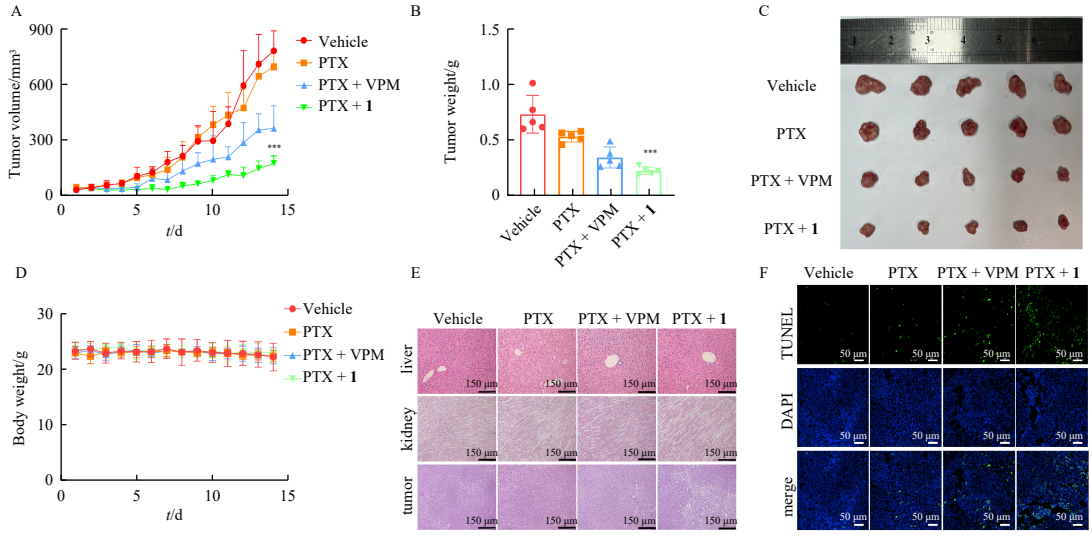


Fig. 9 Effect of **1** on the reversal activity of drug resistance of PTX *in vivo*. (A) Tumor volume of mice was recorded every day during the therapy. (B) Tumor weight after therapy. (C) Photographs of tumors after therapy, compared to the Vehicle group. (D) Body weight of mice was recorded every day. (E) HE staining of tumor, liver, and kidney tissues. The scale bar is 150 μm. (F) TUNEL assay of tumor tissues. The scale bar is 50 μm. Data are presented as the mean ± SD, $n = 3$. $^{***}P < 0.001$ *vs* NC.

automatic polarimeter (Rudolph Research Analytical, Hackettstown, NJ, USA) in CH_3OH. IR spectra were recorded on a Vertex 70 FT-IR spectrophotometer (Bruker, Karlsruhe, Germany). UV spectra were acquired using a PerkinElmer Lambda 35 spectrophotometer (PerkinElmer, Inc., USA). NMR spectra were recorded by a AVANCE NEO 600 NMR spectrometer (Bruker, Karlsruhe, Germany) and AM-400 spectrometer (Bruker, Karlsruhe, Germany). ECD data were acquired using a JASCO-810 instrument (JASCO Co., Ltd., Tokyo, Japan). HRESIMS data were obtained on a Bruker micrOTOF II spectrometer, and the chemical shifts were referenced to the solvent peaks of $CDCl_3$ ($\delta_{H/C}$ 7.26/77.16). The crystallographic data were obtained with an XtaLAB PRO MM007HF equipped with graphite-monochromatized Cu Kα radiation. Melting points were obtained using a Micro melting point instrument (SGW X–4B). An Agilent semipreparative HPLC system with an Ultimate XB-C_{18} column (5 μm, 10 × 250 mm, Welch Ultimate XB-C_{18}) was used to purify these compounds. The packing materials for column chromatography were silica gel (100–200 and 200–300 mesh, Qingdao Marine Chemical Inc., Qingdao, China), ODS (50 μm, YMC, Japan), and Sephadex LH-20 (Pharmacia Biotech AB, Uppsala, Sweden), and the compounds were visualized by spraying silica gel plates with 10% H_2SO_4 in EtOH and heating.

4.2. Fungal material

The fungus *Bipolaris* sp. was obtained from the Agricultural Culture Collection of China with the number ACCC 38958. This strain was cultivated on potato dextrose agar (PDA) medium and authenticated by ITS sequence analysis. The sequence data for this strain have been submitted to GenBank with accession no.PQ771450. The strain was preserved in the culture collection center of Tongji Medical College, Huazhong University of Science and Technology.

4.3. Extraction and isolation

The strain was cultured on PDA medium for 5 days, and then was cut into small pieces and inoculated into 1 L Erlenmeyer flasks, each containing 230 g rice and 230 mL distilled water (total 60 kg rice). Flask cultures were incubated at 28 °C for one month. The fermentation was extracted ten times with aqueous ethanol (EtOH) to yield a residue. The residue was suspended in H_2O and partitioned with ethyl acetate (EtOAc). Then EtOAc residue (1 kg) was isolated by silica gel column chromatography (CC) eluting with petroleum ether (PE, 60–90 °C), EtOAc, and CH_3OH gradient system (from 10∶1∶0 to 5∶5∶2) to obtain five fractions (Fr.1–Fr.5). Fr.3 was separated on an ODS column (CH_3OH–H_2O, 30%–100%) to yield 11 fractions (Fr.3.1–Fr.3.11). Fr.3.8 was subjected to silica gel CC (PE/EtOAc, 15∶1–0∶1) to afford 13 fractions (Fr.3.8.1–Fr.3.8.13). Fr.3.8.11 was further submitted to silica gel CC (PE/EtOAc, 10∶1–0∶1) to get eight fractions (Fr.3.8.11.1–Fr.3.8.11.8). Fr.3.8.11.2 was repeatedly purified by semipreparative HPLC (70% CH_3CN–H_2O, 3.5 mL·min^{-1}) to get compound **1** (10.0 mg, t_R = 44.0 min). Fr.3.8.11.3 was separated by semipreparative HPLC (62% CH_3CN–H_2O, 3.5 mL·min^{-1}) to yield compound **2** (68.0 mg, t_R = 32.0 min). Fr.3.8.5 was isolated by preparative HPLC (70% CH_3CN–H_2O, 10.0 mL·min^{-1}) to get nine fractions (Fr.3.8.5.1–Fr.3.8.5.9). Fr.3.8.5.7 was purified by semipreparative HPLC (82% CH_3OH–H_2O, 3.0 mL·min^{-1}) to get compound **7** (1.0 mg, t_R = 12.0 min). Fr.3.7 was submitted to silica gel CC (PE/EtOAc, 15∶1–0∶1) to obtain 13 fractions (Fr.3.7.1–Fr.3.7.13). Fr.3.7.5 was isolated by semipreparative HPLC (71% CH_3OH–H_2O, 3.0 mL·min^{-1}) to afford compounds **4** (4.0 mg, t_R = 34.0 min) and **6** (4.0 mg, t_R = 32.0 min). Fr.4 was separated on an ODS column (CH_3OH–H_2O, 30%–100%) to yield 19 fractions (Fr.4.1–Fr.4.19). Fr.4.17 was submitted to silica gel CC (CH_2Cl_2/CH_3OH, 100∶1–0∶1) to yield eight fractions (Fr.4.17.1–Fr.4.17.8). Fr.4.17.7 was further isolated by silica gel CC (PE/EtOAc, 10∶1–0∶1) and semipreparative HPLC (73% CH_3OH–H_2O, 3.0 mL·min^{-1}) to get compounds **3** (11.0 mg, t_R = 55.0 min) and **5** (7.0 mg, t_R = 40.0 min)

Kaurepenoid A (**1**): colorless blocks; mp: 137.5–139.0 °C; $[\alpha]_D^{25}$ −96 (*c* 0.1, CH_3OH); UV (CH_3CN) λ_{max} (log ε) = 201 (3.76) nm; ECD (CH_3CN) λ_{max} ($\Delta\varepsilon$) = 203 (+9.23), 226 (−0.84) nm; IR (KBr) ν_{max} 3361, 3191, 2925, 2853, 1819, 1744, 1731, 1660, and 1633 cm^{-1}; ^{1}H NMR ($CDCl_3$, 600 MHz) and ^{13}C NMR ($CDCl_3$, 150 MHz) data, see Table 1; HR-ESI-MS *m/z* 439.2088 [M + Na]$^+$ (Calcd. for $C_{24}H_{32}O_6Na$, 439.2097).

Kaurepenoid B (**2**): colorless blocks; mp: 154.9–156.6 °C; $[\alpha]_D^{25}$ −114 (*c* 0.1, CH_3OH); UV (CH_3CN) λ_{max} (log ε) = 202 (3.75) nm; ECD (CH_3CN) λ_{max} ($\Delta\varepsilon$) = 201 (+10.04), 225 (−0.83) nm; IR (KBr) ν_{max} 3364, 3207, 2927, 2855, 1820, 1733, 1715, and 1659 cm^{-1}; ^{1}H NMR ($CDCl_3$, 400 MHz) and ^{13}C NMR ($CDCl_3$, 100 MHz) data, see Table 1; HR-ESI-MS *m/z* 425.1939 [M + Na]$^+$ (Calcd. for $C_{23}H_{30}O_6Na$, 425.1940).

Kaurepenoid C (**3**): colorless blocks; mp: 91.1–92.5 °C; $[\alpha]_D^{25}$ +16 (*c* 0.1, CH_3OH); UV (CH_3CN) λ_{max} (log ε) = 203 (3.78) nm; ECD (CH_3CN) λ_{max} ($\Delta\varepsilon$) = 204 (+11.73) nm; IR (KBr) ν_{max} 3435, 2928, 2863, 1734, 1442, and 1162 cm^{-1}; ^{1}H NMR ($CDCl_3$, 400 MHz) and ^{13}C NMR ($CDCl_3$, 100 MHz) data, see Table 1; HR-ESI-MS *m/z* 457.2201 [M + Na]$^+$ (Calcd. for $C_{24}H_{34}O_7Na$, 457.2202).

Kaurepenoid D (**4**): colorless blocks; mp: 177.3–178.8 °C; $[\alpha]_D^{25}$ −86 (*c* 0.1, CH_3OH); UV (CH_3CN) λ_{max} (log ε) = 205 (3.53) nm; ECD (CH_3CN) λ_{max} ($\Delta\varepsilon$) = 203 (+7.28) nm; IR (KBr) ν_{max} 3516, 2920, 2852, 1808, and 1656 cm^{-1}; ^{1}H NMR ($CDCl_3$, 400 MHz) and ^{13}C NMR ($CDCl_3$, 100 MHz) data, see Table 2; HR-ESI-MS *m/z* 325.1778 [M + Na]$^+$ (Calcd. for $C_{19}H_{26}O_3Na$, 325.1780).

Kaurepenoid E (**5**): colorless blocks; mp: 164.4–165.6 °C; $[\alpha]_D^{25}$ +12 (*c* 0.1, CH_3OH); UV (CH_3CN) λ_{max} (log ε) = 205 (3.69) nm; ECD (CH_3CN) λ_{max} ($\Delta\varepsilon$) = 204 (+10.96) nm; IR (KBr) ν_{max} 3433, 2925, 2858, 1713, 1668, 1445, 1254, and 1058 cm^{-1}; ^{1}H NMR ($CDCl_3$, 400 MHz) and ^{13}C NMR ($CDCl_3$, 100 MHz) data, see Table 2; HR-ESI-MS *m/z* 357.2053 [M + Na]$^+$ (Calcd. for $C_{20}H_{30}O_4Na$, 357.2042).

Kaurepenoid F (**6**): colorless needles; mp: 171.3–172.5 °C; $[\alpha]_D^{25}$ −163 (*c* 0.1, CH_3OH); UV (CH_3CN) λ_{max} (log ε) = 198 (3.64) nm; ECD (CH_3CN) λ_{max} ($\Delta\varepsilon$) = 218 (−0.90) nm; IR (KBr) ν_{max} 3529, 2931, 2859, 1806, and 1656 cm^{-1}; ^{1}H NMR ($CDCl_3$, 400 MHz) and ^{13}C NMR ($CDCl_3$, 100 MHz) data, see Table 2; HR-ESI-MS *m/z* 325.1780 [M + Na]$^+$ (Calcd. for $C_{19}H_{26}O_3Na$, 325.1780).

Kaurepenoid G (**7**): white powder; $[\alpha]_D^{25}$ −538 (*c* 0.1, CH_3OH); UV (CH_3CN) λ_{max} (log ε) = 200 (4.00) nm; ECD (CH_3CN) λ_{max} ($\Delta\varepsilon$) = 207 (+20.40) nm; IR (KBr) ν_{max} 2925, 2854, 1706, 1472, 1446, and 1063 cm^{-1}; ^{1}H NMR ($CDCl_3$, 600 MHz) and ^{13}C NMR ($CDCl_3$, 150 MHz) data, see Table 2; HR-ESI-MS *m/z* 371.2202 [M + Na]$^+$ (Calcd. for $C_{21}H_{32}O_4Na$, 371.2198).

4.4. X-ray crystal structure analysis

The crystallographic data for compounds **1**–**6** were deposited in the Cambridge Crystallographic Data Centre (CCDC deposition numbers: 2499656, 2499657, 2499658, 2499660, 2499661, and 2499663).

Crystal data for **1**. Colorless blocks (CH_3OH), $C_{24}H_{32}O_6$, M = 416.49, monoclinic, a = 10.28740 (10)Å, b = 8.12190 (10) Å, c = 13.4462 (2) Å, α = 90°, β = 103.5690 (10)°, γ = 90°, V = 1092.12(2) Å^3, T = 293(2) K, space group $P2_1$, Z = 2, μ (Cu Kα) = 0.733 mm^{-1}, F(000) = 448.0, crystal size 0.120 × 0.100 × 0.080 mm^3, 23448 reflections measured, 4323 independent reflections (R_{int} = 0.0482). The final R_1 values were 0.0341 ($I > 2\sigma(I)$). The final $wR(F^2)$ values were 0.0868 ($I > 2\sigma(I)$). The final R_1 values were 0.0347 (all data). The final $wR(F^2)$ values were 0.0871 (all data). The goodness of fit on F^2 was 1.052. Flack parameter =

−0.03(7).

Crystal data for **2**. Colorless blocks (CH_3OH), $C_{23}H_{30}O_6$, M = 402.47, triclinic, a = 6.04860(10)Å, b = 10.85340 (10) Å, c = 16.2161 (2) Å, α = 73.4780(10)°, β = 86.2070(10)°, γ = 89.3120(10)°, V = 1018.34(2) Å^3, T = 296(2) K, space group P1, Z = 2, μ (Cu Kα) = 0. 768 mm^{-1}, F(000) = 432.0, crystal size 0.120 × 0.100 × 0.080 mm^3, 21792 reflections measured, 7708 independent reflections (R_{int} = 0.0562). The final R_1 values were 0.0428 ($I > 2\sigma(I)$). The final $wR(F^2)$ values were 0.1117 ($I > 2\sigma(I)$). The final R_1 values were 0.0445 (all data). The final $wR(F^2)$ values were 0.1132 (all data). The goodness of fit on F^2 was 1.063. Flack parameter = 0.03(11).

Crystal data for **3**. Colorless blocks (CH_3OH), $C_{24}H_{38}O_9$, M = 470.54, monoclinic, a = 6.1750(5) Å, b = 10.3997(9) Å, c = 19.0852(17) Å, α = 90°, β = 91.599(4)°, γ = 90°, V = 1225.14(18) Å^3, T = 104(2) K, space group P2$_1$, Z = 2, μ (Cu Kα) = 0.512 mm^{-1}, F(000) = 508.0, crystal size 0.100 × 0.060 × 0.050 mm^3, 28645 reflections measured, 4845 independent reflections (R_{int} = 0.0721). The final R_1 values were 0.0461 ($I > 2\sigma(I)$). The final $wR(F^2)$ values were 0.1159 ($I > 2\sigma(I)$). The final R_1 values were 0.0491 (all data). The final $wR(F^2)$ values were 0.1174 (all data). The goodness of fit on F^2 was 1.123. Flack parameter = −0.09(9).

Crystal data for **4**. Colorless blocks (CH_3OH), $C_{19}H_{26}O_3$, M = 302.40, monoclinic, a = 9.46340(10) Å, b = 8.25660(10) Å, c = 21.35350(10) Å, α = 90°, β = 100.4690(10)°, γ = 90°, V = 1640.69(3) Å^3, T = 100.00(10) K, space group P2$_1$, Z = 4, μ(Cu Kα) = 0.643 mm^{-1}, F(000) = 656.0, crystal size 0.5 × 0.12 × 0.1 mm^3, 41704 reflections measured, 6458 independent reflections (R_{int} = 0.0443). The final R_1 values were 0.0304 ($I > 2\sigma(I)$). The final $wR(F^2)$ values were 0.0801 ($I > 2\sigma(I)$). The final R_1 values were 0.0307 (all data). The final $wR(F^2)$ values were 0.0803 (all data). The goodness of fit on F^2 was 1.055. Flack parameter = −0.05(6).

Crystal data for **5**. Colorless blocks (CH_3OH), $C_{21}H_{36}O_6$, M = 384.50, orthorhombic, a = 6.40260(10) Å, b = 12.5957(2) Å, c = 25.5115(3) Å, α = 90°, β = 90°, γ = 90°, V = 2057.38(5) Å^3, T = 100.01(10) K, space group P2$_1$2$_1$2$_1$, Z = 4, μ(Cu Kα) = 0.726 mm^{-1}, F(000) = 840.0, crystal size 0.5 × 0.18 × 0.1 mm^3, 31985 reflections measured, 4157 independent reflections (R_{int} = 0.0842). The final R_1 values were 0.0558 ($I > 2\sigma(I)$). The final $wR(F^2)$ values were 0.1433 ($I > 2\sigma(I)$). The final R_1 values were 0.0567 (all data). The final $wR(F^2)$ values were 0.1446 (all data). The goodness of fit on F^2 was 1.024. Flack parameter = 0.03(13).

Crystal data for **6**. Colorless needles (CH_3OH), $C_{19.50}H_{28}O_{3.50}$, M = 318.42, orthorhombic, a = 6.4787(5) Å, b = 19.3669(16) Å, c = 27.380(2) Å, α = 90°, β = 90°, γ = 90°, V = 3435.4(5) Å^3, T = 100(2) K, space group P2$_1$2$_1$2$_1$, Z = 8, μ(Cu Kα) = 0.421 mm^{-1}, F(000) = 1384.0, crystal size 0.100 × 0.020 × 0.010 mm^3, 66709 reflections measured, 6076 independent reflections (R_{int} = 0.1113). The final R_1 values were 0.0781 ($I > 2\sigma(I)$). The final $wR(F^2)$ values were 0.1620 ($I > 2\sigma(I)$). The final R_1 values were 0.0841 (all data). The final $wR(F^2)$ values were 0.1648 (all data). The goodness of fit on F^2 was 1.151. Flack parameter = 0.05(15).

4.5. Synthesis

*4.5.1. Synthesis of compounds **1** and **8**–**11** from compound **2***

Compound **2** (1.3 mg) was divided into several portions and added to a series of 4 mL round-bottom flacks, each containing a dry DCM (CH_2Cl_2, 1.00 mL) solution of EDCI (1-ethyl-3-(3-dimethylaminopropyl)carbodiimide) (1.10 equiv) and DMAP (4-(dimethylamino)pyridine)(0.10 equiv). Then, dry methanol, ethanol, 1-propanol, 1-butanol, and 2-methyl-1-propanol (2.00 equiv) were added to the respective flasks under the Ar. The mixture was stirred at room temperature for 3 h, and the reaction progress was monitored by thin-layer chromatography (TLC). The target compounds were purified by reversed-phase high-performance liquid chromatography (RP-HPLC) using an acetonitrile-water mobile phase (94% CH_3CN) at a flow rate of 3.5 mL·min^{-1}, affording compounds **1** (1.2 mg), **8** (1.1 mg), **9** (1.2 mg), **10** (1.2 mg), and **11** (1.2 mg).

Compound **8**: white powder, 79% yield. ^{1}H NMR (400 MHz, $CDCl_3$) δ_H: 5.22 (1H, dt, J = 11.2, 7.6 Hz), 5.11 (1H, s), 4.79 (1H, dd, J = 6.7, 3.5 Hz), 4.15 (2H, m), 2.62 (4H, m), 2.48 (1H, dd, J = 13.6, 6.9 Hz), 2.44 (1H, m), 2.10 (1H, d, J = 10.6 Hz), 2.01–1.92 (3H, m), 1.73 (3H, d, J = 1.6 Hz), 1.71–1.63 (3H, m), 1.53–1.45 (3H, m), 1.36 (3H, s), 1.39–1.34 (1H, m), 1.26 (3H, t, J = 7.1 Hz), 1.11 (3H, s). HR-ESI-MS m/z 453.2256 [M + Na]$^+$ (Calcd. for $C_{25}H_{34}O_6Na$, 453.2253).

Compound **9**: white powder, 83% yield. ^{1}H NMR (400 MHz, $CDCl_3$) δ_H: 5.22 (1H, dt, J = 11.2, 7.7 Hz), 5.11 (1H, s), 4.79 (1H, dd, J = 6.8, 3.5 Hz), 4.05 (2H, m), 2.62 (4H, m), 2.48 (1H, dd, J = 13.6, 6.8 Hz), 2.44 (1H, m), 2.10 (1H, d, J = 10.6 Hz), 2.01–1.92 (3H, m), 1.73 (3H, d, J = 1.6 Hz), 1.71–1.63 (5H, m), 1.53–1.45 (3H, m), 1.36 (3H, s), 1.39–1.34 (1H, m), 1.11 (3H, d, J = 1.2 Hz), 0.94 (3H, t, J = 7.4 Hz). HR-ESI-MS m/z 467.2418 [M + Na]$^+$ (Calcd. for $C_{26}H_{36}O_6Na$, 467.2410).

Compound **10**: white powder, 81% yield. ^{1}H NMR (400 MHz, $CDCl_3$) δ_H: 5.22 (1H, dt, J = 11.2, 7.7 Hz), 5.11 (1H, s), 4.79 (1H, dd, J = 6.7, 3.5 Hz), 4.09 (2H, m), 2.62 (4H, m), 2.48 (1H, dd, J = 13.6, 6.8 Hz), 2.44 (1H, m), 2.10 (1H, d, J = 10.6 Hz), 2.01–1.92 (3H, m), 1.73 (3H, d, J = 1.6 Hz), 1.71–1.59 (5H, m), 1.53–1.45 (3H, m), 1.36 (3H, s), 1.41–1.34 (3H, m), 1.11 (3H, s), 0.93 (3H, t, J = 7.4 Hz). HR-ESI-MS m/z 481.2568 [M + Na]$^+$ (Calcd. for $C_{27}H_{38}O_6Na$, 481.2566).

Compound **11**: white powder, 81% yield. ^{1}H NMR (400 MHz, $CDCl_3$) δ_H: 5.22 (1H, dt, J = 11.3, 7.7 Hz), 5.11 (1H, s), 4.86 (1H, q, J = 6.3 Hz), 4.79 (1H, dd, J = 6.8, 3.5 Hz), 3.49 (1H, d, J = 4.4 Hz), 2.61 (4H, m), 2.48 (1H, dd, J = 13.8, 7.1 Hz), 2.44 (1H, m), 2.10 (1H, d, J = 10.6 Hz), 2.01–1.92 (3H, m), 1.73 (3H, d, J = 1.6 Hz), 1.72–1.63 (3H, m), 1.61–1.57 (1H, m), 1.54–1.46 (3H, m), 1.36 (3H, s), 1.39–1.34 (1H, m), 1.21 (3H, d, J = 6.3 Hz), 1.11 (3H, d, J = 1.2 Hz), 0.89 (3H, t, J = 7.4 Hz). HR-ESI-MS m/z 481.2566 [M + Na]$^+$ (Calcd. for $C_{27}H_{38}O_6Na$, 481.2566).

*4.5.2. Synthesis of compound **12** from compound **3***

Compound **3** (1.3 mg), K_2CO_3 (2.50 equiv), and CH_3I (2 equiv) were dissolved in anhydrous DMF (1.00 mL) in a 4 mL flask. Anhydrous CH_3OH (2.00 equiv) was then added under Ar. The reaction was stirred at room temperature for 3 h (monitored by TLC), then purified by RP-HPLC (94% CH_3CN/H_2O, 3.5 mL·min^{-1}) to give compound **12** (1.1 mg).

Compound **12**: white powder, 76% yield. ^{1}H NMR (400 MHz, $CDCl_3$) δ_H: 5.23 (1H, dt, J = 11.2, 7.8 Hz), 5.10 (1H, s), 4.17 (1H, q, J = 8.2 Hz), 3.71 (3H, s), 3.69 (3H, s), 2.62 (4H, m), 2.50 (1H, dd, J = 12.1, 6.8 Hz), 2.43 (1H, m), 2.36 (1H, d, J = 8.6 Hz), 2.20–2.14 (2H, m), 1.96 (1H, m), 1.83 (1H, d, J = 8.3 Hz), 1.73 (3H, d, J = 1.6 Hz), 1.75–1.68 (1H, m), 1.62–1.56 (2H, m), 1.42–1.37 (2H, m), 1.36–1.30 (1H, m), 1.25 (3H, s), 1.19 (3H, s), 1.21–1.14 (1H, m). HR-ESI-MS m/z 471.2362 [M + Na]$^+$ (Calcd. for $C_{25}H_{36}O_7Na$, 471.2359).

4.6. Biological assay

4.6.1. Cell lines and culture

SW620/AD300 cell line was provided by Professor Hongmin Liu (Department of Oncology, the Affiliated Cancer Hospital of Zhengzhou University, Zhengzhou, China) and cultivated in Dulbeccos modified Eagle's medium (DMEM) containing 10% fetal bovine serum (Procell Life Science&Technology, Wuhan, China), 100 U·mL^{-1} penicillin, and 100 μg·mL^{-1} streptomycin at 37 °C with 5% CO_2.

4.6.2. Cell counting kit-8 assay

The cells were seeded in 96-well plates at the density of 5 × 10^3 cells per well and preincubated for 24 h. Different concentrations of tested compounds were added into designated wells and incubated for 72 h. Then 10 μL CCK-8 was added to each well and stayed at 37 °C for 1 h. The absorbance of each well was measured at 450 nm using the Varioskan LUX microplate spectrophotometer (Thermo Fisher, Waltham, MA). IC_{50} values were calculated using the GraphPad prism. Reversal fold (RF, the IC_{50} values of PTX divided by PTX/compound combination) was used as a parameter to evaluate the reversal ability of compounds.

4.6.3. Molecular docking

Molecular docking was performed using Schrödinger Maestro (Schrödinger Release 2023-1: Maestro, Schrödinger, LLC, New York, NY, 2023). The protein model 7A6E was obtained from the Protein Data Bank (PDB) and prepared using the Protein Preparation Workflow module. The structure of compound was pre-processed using the LigPrep module. The receptor grid was centered between the substrate-binding site and the access tunnel, fully encompassing both sites. Ligand docking was conducted using default settings. The interactions and alignments were visualized and processed by PyMOL software.

4.6.4. Colony formation assay

SW620/AD300 cells were seeded in 6-well plates (2000 cells/well) and treated with compound **1** combined with different concentrations of PTX for seven days. After removing the medium and washing with PBS, cells were fixed by using 4% paraformaldehyde, stained with 0.1% (*W*/*V*) crystal violet, washed with PBS and then photographed, and counted.

4.6.5. Cell cycle analysis

Cell cycle progression was assessed by flow cytometry. Briefly, SW620/AD300 cells were cultured for 24 h in 6-well plates with compound **1**, after which were collected and fixed overnight at 4 °C in 70% ethanol. Samples were then stained for 30 min with propidium iodide solution containing RNase A, after which they were analyzed with a BD flow cytometer.

4.6.6. Rhodamine123 accumulation assay

SW620/AD300 cells were seeded into 6-well plates (3 × 10^5 cells/well), treated with compound **1** or VPM at 37 °C for 24 h, and then incubated with Rho123 at 37 °C for 30 min. The cells were analyzed with BD FACS flow cytometer.

4.6.7. Cellular thermal shift assay

The membrane protein was extracted from SW620/AD300 cells and divided into two aliquots, one aliquot was treated with DMSO and the other aliquot was treated with compound **1**. After 30 min incubation at 37 °C, the membrane protein was divided into smaller aliquots and then heated at designated temperatures ranging from 40 to 65 °C individually for 3 min. The expression of P-gp in heated membrane proteins was analyzed by western blot.

4.6.8. Xenograft studies

Male BALB/c nude mice (18–22 g, aged 6–7 weeks) were purchased from Vital River Laboratories (VRL, Beijing, China) and housed in ventilated cages and maintained with food and sterile water (ethics approval No. 4881). Approximately 1 × 10^7 SW620/AD300 cells were inoculated subcutaneously into the forelimb of each mouse. The mice were randomized into four groups (n = 5) and treated with one of the following regimens: (i) Vehicle (containing 90% corn oil, and 10% DMSO, 10 mL·kg^{-1}/3 days, i.g.); (ii) PTX (5 mg·kg^{-1}/3 days, dissolved in 10% DMSO and suspended with 90% corn oil, i.g.); (iii) PTX plus VPM (5 mg·kg^{-1}/3 days, dissolved in 10% DMSO and suspended with 90% corn oil, i.g.); (iv) PTX plus **1** (50 mg·kg^{-1}/3 days, dissolved in 10% DMSO and suspended with 90% corn oil, i.g.). The body weight and tumor volume were measured with analytical balance and vernier calipers every day. Following 14-day treatment, animals were euthanized and tumor, liver and kidney tissues were fixed in 4% paraformaldehyde for further analysis.

4.6.9. TUNEL assay

Apoptosis *in vivo* was detected by TUNEL staining. Briefly, tumor tissue sections were incubated with proteinase K for 20 min at room temperature, then were rinsed with PBS. The sections were subsequently incubated with TdT enzyme and FITC-labeled dUTP for 1 h at 37 °C in a humidified chamber. Subsequently, the sections were sealed with antifade mounting medium and the fluorescence of positive staining was examined using a fluorescence microscope.

4.6.10. HE staining

Hematoxylin and eosin (HE) staining was performed for histopathology analysis. Briefly, tissue sections were deparaffinized and stained by hematoxylin for 5 min before being rinsed and differentiated by 1% hydrochloric acid in alcohol (*V*/*V*). Then, the sections were stained in eosin solution for 2 min. After being rinsed and paraffined, the slides were mounted in neutral balsam.

4.6.11. Statistical analysis

All experiments were performed at least in triplicate, and the results are presented as the mean ± standard error (SE). Statistical differences among groups were evaluated by one-way analysis of variance (ANOVA). A value of $P < 0.05$ was considered statistically significant.

Funding

This work was supported by the National Key Research and Development Program of China (No. 2021YFA0910500), the National Natural Science Foundation of China (Nos. U22A20380, 82373755, and 82173706), the Fundamental Research Funds for the Central Universities (Nos. 2024BRA018 and 2025JYCXJJ066), the Natural Science Foundation of Hubei Province (No. 2025AFB227).

Supplementary information

Supplementary data associated with this article can be requested by sending E-mail to the corresponding authors.

Declaration of competing interest

These authors have no conflict of interest to declare.

Acknowledgements

We thank the Analytical and Testing Center and Medical Subcenter at Huazhong University of Science and Technology for assistance in the acquisition of the NMR, ECD, UV, and IR spectra.

References

1 Kibet S, Kimani NM, Mwanza SS, et al. Unveiling the potential of *ent*-kaurane diterpenoids: multifaceted natural products for drug discovery. *Pharmaceuticals*. 2024;17(4):510. https://doi.org/10.3390/ph17040510.
2 Shen YH, Wen ZY, Xu G, et al. Cytotoxic *ent*-kaurane diterpenoids from *Isodon eriocalyx*. *Chem Biodivers*. 2005;2(12):1665-1672. https://doi.org/10.1002/cbdv.200590136.
3 Wang WG, Wu HY, Du X, et al. *Ent*-kaurane diterpenoids from *Isodon eriocalyx* var. *laxiflora*. *Chin J Chem*. 2012;30(6):1226-1230. https://doi.org/10.1002/cjoc.201100653.
4 Zhan R, Li XN, Du X, et al. Bioactive *ent*-kaurane diterpenoids from *Isodon*

rosthornii. *J Nat Prod*. 2013;76(7):1267-1277. https://doi.org/10.1021/np400190n.
5 Liu M, Wang WG, Sun HD, et al. Diterpenoids from *Isodon* species: an update. *Nat Prod Res*. 2017;34(9):1090-1140. https://doi.org/10.1039/c7np00027h.
6 Yue GZ, Liu B. Recent developments in the syntheses of C-20-oxygenated *ent*-kaurane diterpenoids. *ChemPlusChem*. 2024;89:e202300676. https://doi.org/10.1002/cplu.202300676.
7 Xia JN, Hu K, Su XZ, et al. Discovery of *ent*-kaurane diterpenoids, characteristic metabolites of *Isodon* species, from an endophytic fungal strain *Geopyxis* sp. XY93 inhabiting *Isodon parvifolia*. *Fitoterapia*. 2022;158:105160. https://doi.org/10.1016/j.fitote.2022.105160.
8 Chen SP, Hu K, Dong XX, et al. Discovery and semisynthesis of aurantiacin A: a unique ascorbylated 9-*epi*-*ent*-kaurane diterpenoid from the untapped plant *Isodon aurantiacus*. *Org Lett*. 2025;27:3883-3888. https://doi.org/10.1021/acs.orglett.5c00586.
9 Yang J, Wang WG, Wu HY, et al. *Ent*-kaurene diterpenoids from *Isodon phyllostachys*. *Tetrahedron Lett*. 2017;58(4):349-351. https://doi.org/10.1016/j.tetlet.2016.12.034.
10 Li SH, Wang J, Niu XM, et al. Maoecrystal V, cytotoxic diterpenoid with a novel C19 skeleton from *Isodon eriocalyx* (Dunn.) Hara. *Org Lett*. 2004;6(23):4327-4330. https://doi.org/10.1021/ol0481535.
11 Fan YY, Shi SQ, Deng GZ, et al. Crokonoids A–C, a highly rearranged and dual-bridged spiro diterpenoid and two other diterpenoids from *Croton kongensis*. *Org Lett*. 2020;22(3):929-933. https://doi.org/10.1021/acs.orglett.9b04484.
12 Zhu LZ, Ma WJ, Zhang MX, et al. Scalable synthesis enabling multilevel bio-evaluations of natural products for discovery of lead compounds. *Nat Commun*. 2018;9(1):1283. https://doi.org/10.1038/s41467-018-03546-9.
13 Kılıç T, Topcu G, Goren AC, et al. *Ent*-kaurene diterpenoids from *Sideritis lycia* with antiviral and cytotoxic activities. *Rec Nat Prod*. 2020;14(4):256–268. https://doi.org/10.25135/rnp.163.19.08.1373.
14 Silva ML, Oliveira CS, Dos Santos WJO, et al. Selective cytotoxicity of *ent*-kaurene diterpenoids isolated from *Baccharis lateralis* and *Baccharis retusa* (Asteraceae). *Arch Pharm*. 2022;355(8):e2200083. https://doi.org/10.1002/ardp.202200083.
15 Li DH, Hu X, Han T, et al. Synthesis, biological activity, and apoptotic properties of NO-donor/enmein-type *ent*-kauranoid hybrids. *Int J Mol Sci*. 2016;17:747. https://doi.org/10.3390/ijms17060747.
16 Nguyen TVA, Nguyen TMH, Le HL, et al. Antithrombotic activity of the steroids and *ent*-kaurane diterpenoids from *Canna indica* Rhizomes. *Rev Bras Farmacogn*. 2024;34(1):206-211. https://doi.org/10.1007/s43450-023-00472-w.
17 Xing H, An L, Song Z, et al. Anti-inflammatory *ent*-kaurane dterpenoids from *Isodon serra*. *J Nat Prod*. 2020;83(10):2844-2853. https://doi.org/10.1021/acs.jnatprod.9b01281.
18 de Lima EJSP, Paz WHP, Dávila Cardozo NM, et al. Anti-biofilm and anti-inflammatory active diterpene isolated from the fruit of *Xylopia benthamii* R. E.Fr. *Nat Prod Res*. 2024;38:956-967. https://doi.org/10.1080/14786419.2023.2208357.
19 Wang YL, Jiang QH, Sun DJ, et al. *Ent*-kauranes and *ent*-atisanes from *Euphorbia wallichii* and their anti-inflammatory activity. *Phytochemistry*. 2023;210:113643. https://doi.org/10.1016/j.phytochem.2023.113643.
20 Selener MG, Borgo J, Sarratea MB, et al. Trypanocidal and anti-inflammatory effects of three *ent*-kaurane diterpenoids from *Gymnocoronis spilanthoides* var. *subcordata* (Asteraceae). *Pharmaceutics*. 2024;16(3):415. https://doi.org/10.3390/pharmaceutics16030415.
21 Wang G, Ding AX, Qin GQ, et al. Dimeric *ent*-kauranoids isolated from *Isodon japonica* var. *Glaucocalyx* and their anti-inflammatory activities. *Fitoterapia*. 2024;174:105840. https://doi.org/10.1016/j.fitote.2024.105840.
22 Liu WH, Chen J, Wu L, et al. Anti-inflammatory diterpenoids from the aerial parts of *Isodon suzhouensis*. *ACS Omega*. 2025;10:16658-16667. https://doi.org/10.1021/acsomega.5c00223.
23 Moritz BJ, Mack DJ, Tong L, et al. Total synthesis of the *Isodon* diterpene sculponeatin N. *Angew Chem Int Ed*. 2014;53(11):2988-2991. https://doi.org/10.1002/anie.201310060.
24 Zhang WB, Shao WB, Li FZ, et al. Asymmetric total synthesis of (−)-maoecrystal V. *Chem Asian J*. 2015;10(9):1874-1880. https://doi.org/10.1002/asia.201500564.
25 He C, Hu JL, Wu YB, et al. Total syntheses of highly oxidized *ent*-kaurenoids pharicin A, pharicinin B, 7-*O*-acetylpseurata C, and pseurata C: a [5 + 2] cascade approach. *J Am Chem Soc*. 2017;139(17):6098-6101. https://doi.org/10.1021/jacs.7b02746.
26 Liu JS, Luo LP, Xu G, et al. Synthesis and biological evaluation of steviol derivatives with improved cytotoxic activity and selectivity. *J Nat Prod*. 2022;85(8):1945-1958. https://doi.org/10.1021/acs.jnatprod.2c00161.
27 Santana VCS, Rocha ECS, Pavan JCS, et al. Selective oxidations in the synthesis of complex natural *ent*-kauranes and *ent*-beyeranes. *J Org Chem*. 2022;87(15):10462-10466. https://doi.org/10.1021/acs.joc.2c01051.
28 Xu C, Ou E, Li ZY, et al. Synthesis and *in vivo* evaluation of new steviol derivatives that protect against cardiomyopathy by inhibiting ferroptosis. *Bioorg Chem*. 2022;129:106142. https://doi.org/10.1016/j.bioorg.2022.106142.
29 Gu Q, Walby GD, Wood MD, et al. Total synthesis of (+)-pierisketone B. *J Am Chem Soc*. 2025;147:29631-29635. https://doi.org/10.1021/jacs.5c08617.
30 Lu P, Mailyan A, Gu ZH, et al. Enantioselective synthesis of (−)-maoecrystal V by enantiodetermining C–H functionalization. *J Am Chem Soc*. 2014;136:17738-17749. https://doi.org/10.1021/ja510573v.
31 Zhang JP, Li ZJ, Zhuo JM, et al. A tandem decarboxylative cyclization/alkenylation strategy for the total syntheses of (+)-longirabdiol, (−)-longirabdolactone, and (−)-lffusin. *J Am Chem Soc*. 2019;141:8372-8380. https://doi.org/10.1021/jacs.9b03978.
32 Cao ZC, Sun WX, Zhang JF, et al. Total syntheses of (−)-macrocalyxoformins A and B and (−)-ludongnin C. *Nat Commun*. 2024;15:6052. https://doi.org/10.1038/s41467-024-50374-1.
33 Shen Y, Li Q, Ding NJ, et al. Bipoladisins A–G, uncommon sesterterpenoids with three types of carbon skeletons from *Bipolaris maydis* and their reversal activity on paclitaxel resistance. *J Nat Prod*. 2025;88:1286-1297. https://doi.org/10.1021/acs.jnatprod.5c00024.
34 Liu X, Xu JM, Zhou J, et al. Oridonin and its derivatives for cancer treatment and overcoming therapeutic resistance. *Genes Dis*. 2021;8:448-462. https://doi.org/10.1016/j.gendis.2020.06.010.
35 He ZW, Xiao XL, Li S, et al. Oridonin induces apoptosis and reverses drug resistance in cisplatin resistant human gastric cancer cells. *Oncol Lett*. 2017;14:2499-2504. https://doi.org/10.3892/ol.2017.6421.
36 Li ZH, Ai HL, Yang MS, et al. Bioactive sativene sesquiterpenoids from cultures of the endophytic fungus *Bipolaris eleusines*. *Phytochem Lett*. 2018;27:87-89. https://doi.org/10.1016/j.phytol.2018.07.007.
37 Wang XJ, Wang Z, Han J, et al. Sativene sesquiterpenoids from the plant endophytic fungus *Bipolaris victoriae* S27 and their potential as plant-growth regulators. *J Agric Food Chem*. 2024;72:2598-2611. https://doi.org/10.1021/acs.jafc.3c05815.
38 Shu Y, Feng SY, Zhang SQ, et al. Bipodonines A–J, a new class of natural sesquiterpenes with a 2-(tetrahydro-2*H*-pyran-2-yl)propan-2-ol system from the fungus *Bipolaris cynodontis* DJWT-01. *Org Chem Front*. 2023;10:2442-2452. https://doi.org/10.1039/d3qo00235g.
39 Wang QX, Qi QY, Wang K, et al. Coicenals A–D, four new diterpenoids with new chemical skeletons from the plant pathogenic fungus *Bipolaris coicis*. *Org Lett*. 2013;15:3982-3985. https://doi.org/10.1021/ol401736z.
40 Liu MT, Sun WG, Shen L, et al. Bipolaricins A–I, ophiobolin-type tetracyclic sesterterpenes from a phytopathogenic *Bipolaris* sp. fungus. *J Nat Prod*. 2019;82:2897-2906. https://doi.org/10.1021/acs.jnatprod.9b00744.
41 Shen Y, Chen CM, Zhao ZM, et al. Bipoladien A, a sesterterpenoid containing an undescribed 5/8/5/7 carbon skeleton from *Bipolaris maydis*. *J Agric Food Chem*. 2024;72:3549-3559. https://doi.org/10.1021/acs.jafc.3c08134.
42 Shen Y, Ding NJ, Gu LH, et al. Maydisens, sesterterpenoids with anti-MDR activity from *Bipolaris maydis*. *J Nat Prod*. 2024;87:2408-2420. https://doi.org/10.1021/acs.jnatprod.4c00658.
43 Liu MT, Zhang XK, Shen L, et al. Bioactive polyketide-terpenoid hybrids from a soil-derived fungus *Bipolaris zeicola*. *J Org Chem*. 2021;86:10962-10974. https://doi.org/10.1021/acs.joc.0c02237.
44 Han JY, Zhang JY, Song ZJ, et al. Genome-based mining of new antimicrobial meroterpenoids from the phytopathogenic fungus *Bipolaris sorokiniana* strain 11134. *Appl Microbiol Biotechnol*. 2020;104:3835-3846. https://doi.org/10.1007/s00253-020-10522-1.
45 Fan YZ, Tian C, Tong SY, et al. The antifungal properties of terpenoids from the endophytic fungus *Bipolaris eleusines*. *Nat Prod Bioprospect*. 2023;13:43. https://doi.org/10.1007/s13659-023-00407-x.
46 Tran TMD, Nguyen VK, Duong TH, et al. Maydisone, a novel oxime polyketide from the cultures of *Bipolaris maydis*. *Nat Prod Res*. 2020;36:102-107. https://doi.org/10.1080/14786419.2020.1765339.
47 Fan YZ, Tian C, Tong SY, et al. Chromones from the endophytic fungus *Bipolaris eleusines*. *Phytochemistry*. 2024;221:114046. https://doi.org/10.1016/j.phytochem.2024.114046.
48 Liu MT, Zhang XK, Shen L, et al. Meroterpenoids with potent immunosuppressive activity from fungus *Bipolaris zeicola*. *Chin J Chem*. 2021;39:2460-2466. https://doi.org/10.1002/cjoc.202100233.
49 Liu MT, Gu LH, Shen L, et al. Bipolaquinones A–J, immunosuppressive meroterpenoids from a soil-derived *Bipolaris zeicola*. *J Nat Prod*. 2021;84:2427-2436. https://doi.org/10.1021/acs.jnatprod.1c00327.
50 Duan XY, Tan XS, Gu LH, et al. New secondary metabolites with immunosuppressive activity from the phytopathogenic fungus *Bipolaris maydis*. *Bioorg Chem*. 2020;99:103816. https://doi.org/10.1016/j.bioorg.2020.103816.
51 Yin Q, Han JY, Yang GX, et al. New sesquiterpenoids with anti-inflammatory effects from phytopathogenic fungus *Bipolaris sorokiniana* 11134. *Nat Prod Bioprospect*. 2025;15:29. https://doi.org/10.1007/s13659-025-00508-9.
52 Zhao XL, Niu YC, Deng H, et al. Characterization and phytotoxicity of ophiobolins produced by *Bipolaris setariae*. *Mycoscience*. 2021;62:64-70. https://doi.org/10.47371/mycosci.2020.11.002.
53 Nishimura K, Hitotsuyanagi Y, Sakakura KI, et al. Three new diterpenoids, tricalysiolide H and tricalysiones A and B, from *Tricalysia dubia*. *Tetrahedron*. 2007;63(21):4558-4562. https://doi.org/10.1016/j.tet.2007.02.113.
54 Stadler M, Bitzer J, Mayer-Bartschmid A, et al. Cinnabaramides A–G: analogues of lactacystin and salinosporamide from a *Terrestrial streptomycete*. *J Nat Prod*. 2007;70:246-252. https://doi.org/10.1021/np060162u.
55 Li Y, Xue QL, Zhao XB, et al. Total syntheses of diepoxy-*ent*-kaurane diterpenoids enabled by a bridgehead-enone-initiated intramolecular cycloaddition. *J Am Chem Soc*. 2025;147:1197-1206. https://doi.org/10.1021/jacs.4c15004.